# A Stray-Field-Immune Magnetic Displacement Sensor With 1% Accuracy

Nicolas Dupré, Yves Bidaux, Olivier Dubrulle, and Gael F. Close, *Senior Member, IEEE*

***Abstract*—We present a new Hall sensor design for the accurate and robust measurement of linear displacement. Implemented in CMOS, the sensor is based on a novel gradient measurement concept combining Hall elements with integrated magnetic concentrators. In typical applications with practical Ferrite magnets, the peak output voltage of the Hall transducers is only around 1.7 mV at the maximum operating temperature of 160°C, and thus requires high-performance low-offset readout electronics. Over its 15-mm linear displacement range, the sensor's total error is 1% including manufacturing tolerances, trimming accuracy, temperature, aging effects, and practical magnet constraints. In addition, the sensor is immune to magnetic stray fields up to 5 mT, complying with the most stringent automotive norm.**

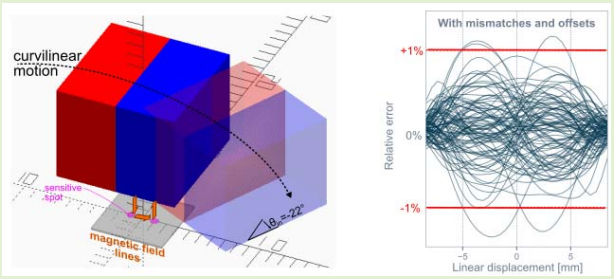


***Index Terms*— Automotive electronics, Hall effect, magnetic sensors.**

## I. Introduction

ABOUT 6 billions semiconductor magnetic sensors are shipped each year [1]. Magnetic sensors cover a range of technologies: Hall, AMR, GMR, TMR, magneto-inductive and others. They serve numerous applications such as compass, position (angle, linear displacement), and current sensing. Automotive applications accounts for about half of the market [1]. Due to the electrification of vehicles, magnetic stray fields are increasingly present. For example in [2], magnetic fields of several hundreds of μT were measured in electric vehicles, and traced to traction currents. Such level of stray field would corrupt any accurate magnetic sensor measurement if left unmitigated. We focus here on compact linear displacement sensor with a full-stroke above 10 mm. This is by contrast to close proximity sensors where the full-scale range is limited to a few millimeters, but with sub-nanometer resolution [3].

We target space-constrained applications requiring "PCB-less" point-like sensors. There is no physical space for a long distributed transducer covering the range of motion. This excludes magnetostrictive and magneto-inductive sensors. With both of these technologies, the magnet position is transduced into a localized change of a material property. And this is sensed electrically either as a change of pulse delay [4], or as a change of impedance [5], [6]. The active transducer length is then commensurate with the range of motion: the magnet slides along the transducer, and the transducer is distributed and not point-like. For the same reason inductive sensors are not suitable despite being robust to low-frequency stray fields by the virtue of their operation at several MHz. The nonlinearity of the B-H curve of the ferromagnet core, if present, limits the rejection [7].

This leaves us with point-like magnetic field sensors based on Hall effect [8] or magnetoresistive effects. They provide point-like field measurements, a proxy for the mechanical position of the magnet. The magnetoresistive sensors are especially attractive thanks to their high intrinsic sensitivity [9]. They work directly in the angle domain, which is an advantage in angle sensing. However, this complicates largely the rejection of stray fields [10]. The stray field rotates in a non-linear way the sensed angle, and this error cannot simply be canceled by differential sensing.

We previously demonstrated an angle sensor immune to stray fields [11] based on differential field sensing. This is not a complete immunity, just a rejection up to the degree specified by international standard [12]. Angle sensing plays a major role in engine control, steering, and numerous other applications (pedal, wipers, …). Besides angle sensing, linear displacement sensors are also of interest for a variety of automotive applications, for example shift-by-wire and brake booster with physical space at a premium.

In this paper, we generalize our previous work by developing a compact Hall-based linear displacement sensor suitable for operation in harsh automotive environment. We give an

Manuscript received April 30, 2020; accepted May 16, 2020. Date of publication May 28, 2020; date of current version September 3, 2020. The associate editor coordinating the review of this article and approving it for publication was Prof. Boby George. *(Corresponding author: Gael F. Close.)*

Nicolas Dupré, Yves Bidaux, and Gael F. Close are with Melexis, 2022 Bevaix, Switzerland (e-mail: ndp@melexis.com; ybi@melexis.com; gcl@melexis.com).

Olivier Dubrulle is with Melexis, 8900 Ypres, Belgium (e-mail: odu@melexis.com).

Digital Object Identifier 10.1109/JSEN.2020.2998289

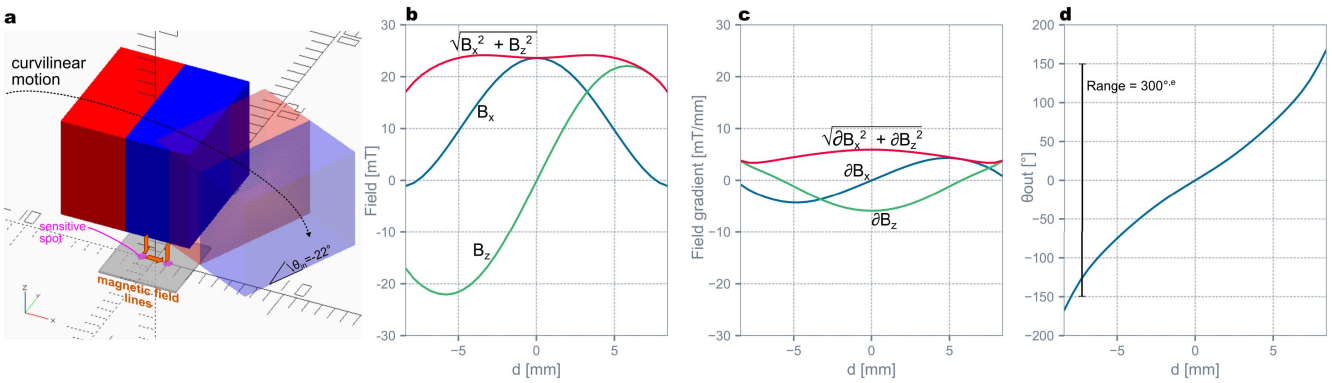


Fig. 1. Magnetic concept. (a) Curvilinear motion of a two-pole magnet along an arc over the sensor. (b) Magnetic field components as function of the displacement. (c) Gradient components of interest. (d) Resulting sensor transfer curve from the mechanical displacement to the sensed electrical angle.

overview of our concept in section II. Section III describes the electronic design. Section IV provides implementation details. The experimental results are presented in section V, and discussed in section VI.

## II. Magnetic Sensing Concept

### A. Mechanical Stroke and Magnetic Fields

The magnetic concept is illustrated in Fig. 1. We consider a general curvilinear displacement of a two-pole magnet along an arc above a Hall sensor. In this specific example, we have $r_{\text{arc}} = 20$ mm for the arc radius and $\Delta\theta_{\text{in}} = \pm 22°$ for the mechanical angle range. In terms of linear displacement $d$, the range is then $d_{\text{range}} = r_{\text{arc}} \cdot \Delta\theta_{\text{in}} \approx \pm 7.5$ mm. The magnetic field lines above the sensor are arching in a U-shaped pattern. When the sensor is centered under the axis of symmetry of the magnet, the magnetic field lines are in the sensor plane, and the field component $B_x$ dominates. As the magnet moves sideways, an out-of-plane component $B_z$ arises. The field components as a function of the magnet motion are shown in Fig. 1b. These plots were calculated by a magnetic simulation tool we discussed before [13]. In order to reject any potential interfering stray field, the sensor measures instead the gradient component $\partial B_x/\partial x$ and $\partial B_z/\partial x$. They are plotted in Fig. 1c. Unlike in the classical angle sensor case, the waveforms are not simple sine waves. The electrical angle extracted from these two raw components is then a non-linear function of the mechanical angle. The overall transfer function of the sensor from the linear displacement $d$ to the electrical output angle $\theta_{\text{out}}$ is shown in Fig. 1d. The 15-mm linear displacement range is mapped, non linearly, to an electrical angular range of $300^{\text{o,electrical}}$. We use the suffix *electrical* to distinguish this electrically-sensed angle from the mechanical angle defining the position along the arc. The overall non-linearity is a static error, and can be readily compensated in the embedded software by a calibration. The residual dominant errors are due to thermal and lifetime drift.

### B. Error Model

In order to gain insight into the trade-off, we derive a simplified analytical model. Consider a Ferrite cubic magnet

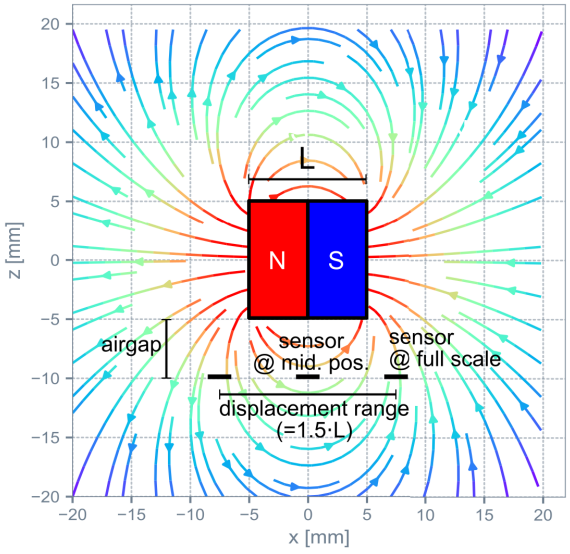


Fig. 2. Geometry and magnetic field lines for a cube magnet.

of length $L = 10$ mm with magnetization along the x-axis ($B_r = 350$ mT). Fig. 2 shows the magnetic field pattern from such magnet as calculated by the Magpylib library [14]. The displacement range $d_{\text{range}}$ is limited to about 1.5 times the magnet length: $d_{\text{range}} = 1.5 \cdot L$ to preserve some margin against the angle wrap-around behavior. Assuming an airgap of 5 mm, the field $B_x$ at the sensor location is $B_x \approx 24$ mT and its gradient $\partial B_x/\partial x \approx 6$ mT/mm. Considering the characteristic dimension of the chip, we can define the following dimensionless ratio $B/\Delta B$:

$$B/\Delta B = \frac{|B|}{\sqrt{\left(\frac{\partial B_x}{\partial x}\right)^2 + \left(\frac{\partial B_z}{\partial x}\right)^2} \cdot 1\ mm}. \tag{1}$$

Longer magnets naturally allow longer range. However, these longer magnets increasingly generate a uniform field with limited gradient. In other words, for longer range the ratio $B/\Delta B$ increases. At the center position, the common-mode field $B_x$ increasingly dominates over the signal gradient.

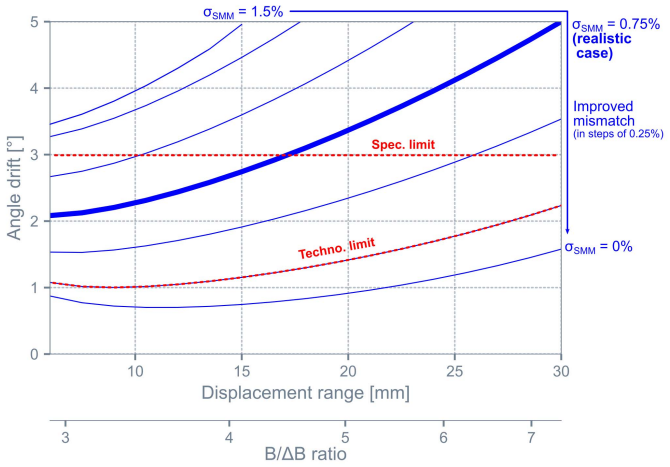


Fig. 3. Trade-off curve. Angle drift as a function of the displacement range assuming different sensitivity mismatch.

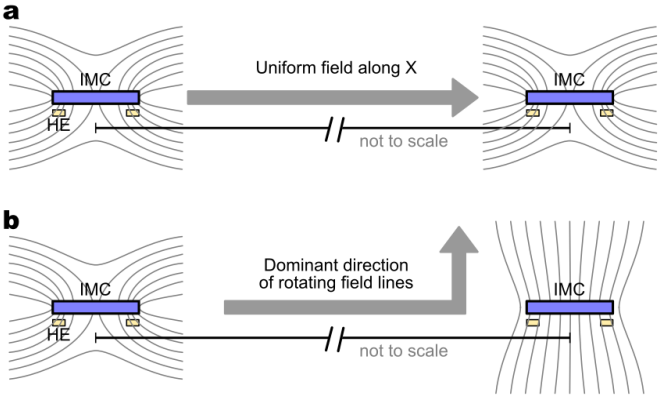


Fig. 4. Sensor cross-section through the two disks and magnetic field lines: (a) when the magnet is centered above the sensor, (b) when the magnet is displaced sideways to the left such that the right disk is under a pole.

In the presence of sensitivity mismatch $\sigma_{SMM}$, the common-mode field leaks into the signal path, yielding a standard error equal to $\sigma_{\text{SMM}} B_x$. In addition, there is also an offset error impacting each Hall element (HE) with standard deviation $\sigma_{\text{Offset}} = 50\ \mu\text{T}$. Both error sources are to be summed in root sum square (RSS) fashion. The total error relative to the signal amplitude yields the angular error. As there is a calibration in the final module at room temperature, what matters is the drift after this calibration. Fig. 3 illustrates the trade-off between range and accuracy. The angle drift is plotted as a function of the displacement range for various sensitivity mismatches. The feasible region in terms of angle drift is bounded on the high side by the specification limit, and on the low side by the technological limit. We assume a typical automotive specification limit of 1% corresponding to $3^{\circ,\text{electrical}}$. In the plot, we assumed that the ultimate technological limit is such that $\sigma_{\text{SMM}} = 0.25\%$. The practical realistic mismatch is higher. Some level of residual mismatch is expected given that the sensitive HEs have to be spaced at least 1 mm apart to sense significant field differences. This is the nature of gradient sensing: it requires spatial spreading, and hence significant mismatches are to be expected.

## III. Electronic Design

### A. Differential Sensing

To sense $B_x$ and $B_z$, integrated magneto concentrator (IMC) disks are post-processed on the chip surface. Each IMC disk (other shapes would also work) deflects the field lines, thereby allowing the use of a pair of horizontal HEs to measure $B_x$ and $B_z$ [15] depending on the sign of the combination. For differential sensing, two disks, one on each side of the sensor, are used. The left and right disk measurements are then combined differentially to measure $\partial B_x/\partial x$ and $\partial B_z/\partial x$. Fig 4a depicts the situation when the magnet is centered. The field lines are along the x-axis. This common-mode field component is rejected by the differential sensing scheme. On the contrary, when the magnet is off-centered close to the extremes of the displacement range, the field lines are curved (Fig 4b), and a differential signal appears.

### B. Electrical Signal Chain

The signal chain is based on a previously-discussed generic platform [16]. Fig. 5 shows the block diagram for this specific sensing mode. At the maximum temperature 160 °C, the magnet strength has dropped ($\text{temp.co}_{\text{Ferrite}} = -2000$ ppm/°C), the gradient is only 4.5 mT/mm. The sensed Hall voltage sum at the input of the electronic signal chain reaches about 1.7 mV. Offsets are mitigated thanks to a combination of 4-phase current spinning, effectively chopping the signal, and a fine correction in software. The offset correction is calibrated at the factory at multiple temperatures. The software performs the correction based on real-time readout of the chip temperature and interpolation. Residual offsets [17] are below 5 µV (standard deviation) at 160 °C after accelerated life testing. The Hall voltages are summed in the current domain after a transconductance amplification stage and appropriate sign inversion $a_k = \pm 1$. The resulting signal is then amplified, filtered and converted to digital codes.

The rest of the signal chain is implemented by an embedded software algorithm. It performs unchopping, applies the factory-calibrated corrections, and calculates the angle. The embedded software also performs closed-loop gain and centering adjustments to avoid saturation. A final non-linearity (NL) correction is also included. The calibration of the NL correction is performed by the final user in the final assembled module (consisting of the sensor chip and the magnet). This is because these calibration coefficients depend on the mechanical and magnetic application details. The corrected angle is then transmitted as an analog voltage or as a digital frame using standard automotive digital protocols.

### C. Hall Plate Biasing and Readout

Given that the sensitivity mismatches $\delta S_k$ between HEs are critical, special attention is needed to their biasing and readout. Fig. 6 shows the biasing and readout circuit. A reference current is generated by a reference bias voltage imposed across a reference HE. This reference current is then mirrored into the active sensing HEs, possibly with digital fine tuning. The variability associated with the resistance spread is then

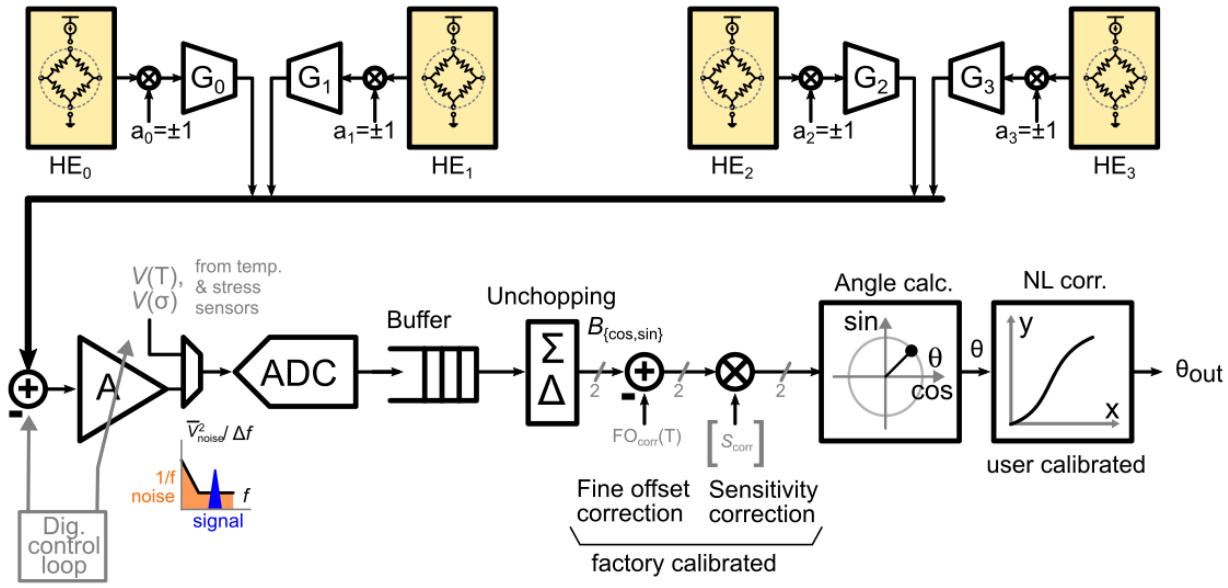


Fig. 5. Sensor block diagram.

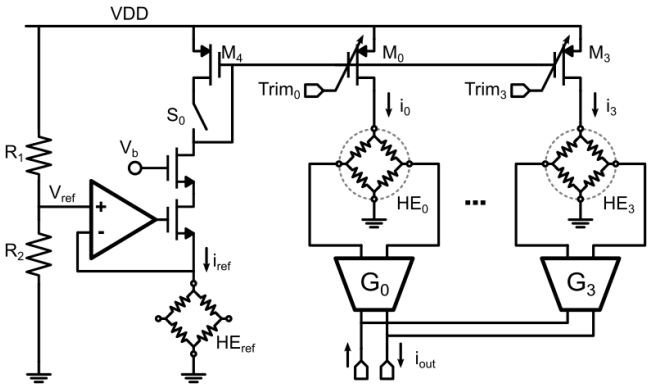


Fig. 6. Hall element bias and readout circuit.

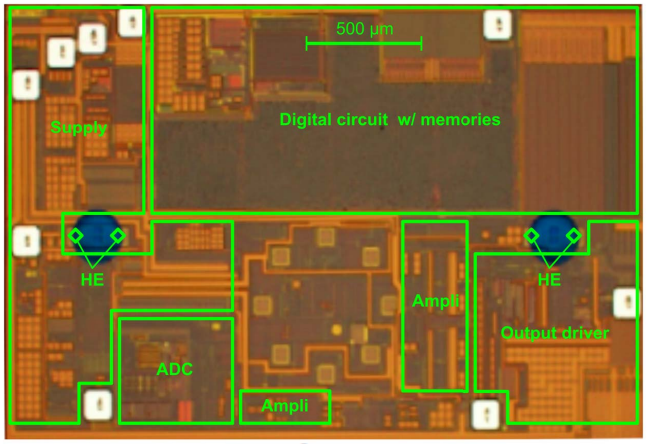


Fig. 7. Chip photograph. The blue disks are the IMC disks that have been micro-machined on top of the CMOS wafers.

mitigated. Alternatively, the switch $S_0$ when open, disables the current mirrors and instead transistors $M_0 \ldots M_3$ operate as closed switches, applying the maximum voltage to the HEs.

The Hall voltages are converted to currents by matched transconductance amplifier stages $G_k$, and summed in the current domain. Note that the mismatch is dominated by the HEs and not the amplifiers $G_k$. Consequently, dynamic element matching techniques to swap the $G_k$ stages would only provide a marginal improvement. As alluded before, some level of residual mismatch is naturally to be expected given that the sensitive HEs have to be spaced apart to sense field difference. Over the relevant scale, chip bending [18] and stress gradient contribute to residual mismatches.

## IV. Implementation

The design is implemented in a CMOS 0.18-$\mu$m technology. The HEs are covered by IMC disks post-processed at the wafer level [15]. Fig. 7 shows the chip micrograph after IMC post-processing. The chip is a standalone smart sensor. It includes a digital microcontroller running the embedded software. The chip is automotive qualified, and supports harsh environment. The operating temperature can reach up to 160 °C, with absolute maximum voltage rating of 28 V. The chip complies with stringent EMC and ESD requirements calling for a robust power supply and output driver.

## V. Results

### A. Drift of Key Parameters

About 100 production samples were subjected to AEC-Q100 qualification tests to emulate the lifetime mission profile. The measured drift of the two key parameters is plotted in Fig. 8. The offset software correction, which was factory calibrated, remains effective even at the end of lifetime. The standard deviation of the residual offset after embedded software correction at 160 °C was below 5 µV (by contrast: 20 µV without software correction). To characterize the sensitivity mismatches $\delta S_k$, and capture how much common-mode leaks into the signal, we define a common

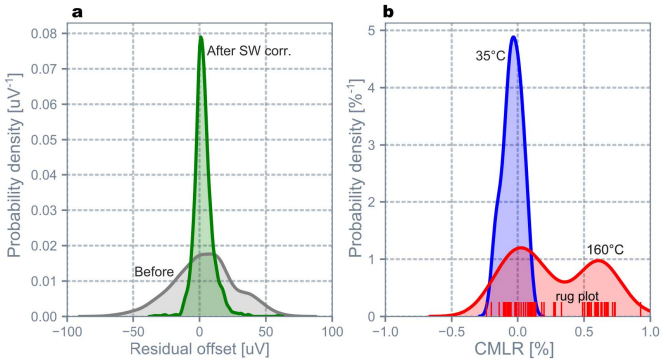


Fig. 8. Empirical probability density functions extracted from 96 chips after 408 hours of operation at 175°C to emulate the lifetime (the y-axis units are such that the area under the curves are 1). (a) Input-referred offset voltage at 160°C before and after software correction. (b) Change, over temperature and lifetime, of the common-mode leakage ratio of the HE sensitivities. The actual 96 measurements at 160°C are showed as marks along the x-axis (rug plot).

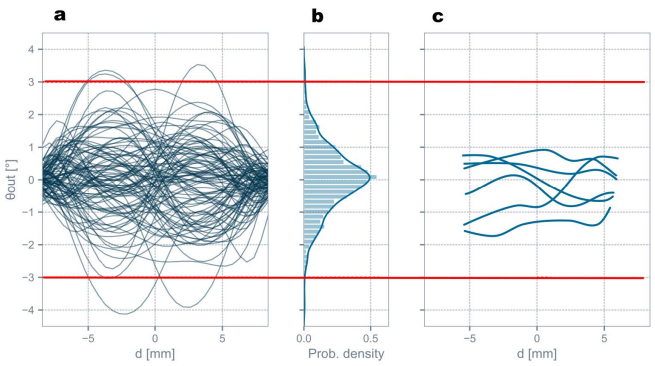


Fig. 9. Experimental validation. (a) Simulated angle drift curves by Monte Carlo technique for 100 chips at 135°C. (b) Corresponding simulated distribution. (c) Empirically measured angle drift curves of 6 sample chips at 135°C assembled in final application modules. The common horizontal red lines denotes the ±3° specification limits.

mode leakage ratio CMLR.

$$\mathrm{CMLR} = \frac{\sum_k \delta S_k a_k}{\sum_k S_k}. \tag{2}$$

It can be viewed as the inverse of the traditional common-mode rejection ration. Over the whole sample population ($N = 96$) the drift of CMLR remained $< 1\%$.

### B. Angle Drift in Application

Production samples have been characterized using multi-pole electromagnets with almost zero common-mode field. Although this gives insight into the IC intrinsic lab performance, this is not representative of practical applications. To account for the common-mode field, the offset and mismatch statistics measured above were re-injected into a Monte Carlo simulation including realistic magnetic stimulus. Fig. 9a depicts the simulated angle drift curves at 135 °C for a configuration like in Fig. 1. The corresponding simulated probability density function is shown in Fig.9b. The expected 3-sigma limit is about 1%. To validate these simulations, 6 random samples were assembled in a module with a 2-pole magnet like in Fig. 1. Fig. 9c shows the measured angle drift at 135 °C. The angle drift on all 6 samples remained well below 1%.

## VI. Discussion

To finalize the error budget, additional secondary errors need to be accounted for. First the user calibration is not ideal. Practically, there is a residual error of up to ±0.2°. We assume, conservatively, that the probability distribution is uniform. Second, there could be a stray field of up to 5 mT [12]. Just like the common-mode field, it leaks into the signal path via sensitivity mismatches. The stray-field-induced error was experimentally characterized in a handful of samples. The error remained below 0.2°. To understand the probability distribution limits, we again ran Monte Carlo simulations including mismatches. Error of up to ±0.8° were observed in simulation (3 sigma, Normal distribution assumed as this effect is related to mismatches). Table I summarizes the static error budget expressed in electrical degree. The errors are all standardized, and combined in RSS fashion to obtain the final total static error of ±3.1° (Normal distribution, 3 sigma). This is equivalent to 1% for the assumed range of 300°. For dynamic application, noise should be included. The noise is dominated by the thermal noise arising from the HE resistance ≈ 20 kΩ (corresponding to about 2 $\mu$V,rms in a 10 kHz bandwidth) at the maximum temperature, and not by the electronic readout chain. Noise adds an extra standard error of $0.15^{\circ,\mathrm{rms}}$.

Table II compares our results against other Hall-based automotive linear displacement sensors. The first one is another dual pixel sensor, but based on a combination of horizontal and vertical Hall devices. Historically, vertical Hall devices have suffered from significantly lower sensitivity and larger offsets [19], although state-of-the art devices are narrowing the gap [20]. The larger offset degrades the accuracy at low magnetic field amplitude (like the field amplitude generated by a small

TABLE I
Error Budget for the Total Static Error

| Error source | Limits | Distri. | Divisor | Std. err. |
|---|---|---|---|---|
| Residual NL after cal. | ±0.2° | Uniform | $\sqrt{3}$ | 0.11° |
| Stray-field error @5mT | ±0.8° | Normal | 3 | 0.27° |
| Drift[1] | ±3.0° | Normal | 3 | 1.00° |
| | | | Total std. error | 1.04° |
| | | | Total error ($3\sigma$) | 3.12° |

[1] Thermal and lifetime drift.

TABLE II
Comparison Between This Work and Other Hall-Based Displacement Automotive Sensors

| | This work | [22] | [21] |
|---|---|---|---|
| Nr. of sensor chips | 1 | 1 | 2 |
| Hall technology | Horiz. and IMC | Horiz. | Vert. and horiz. |
| $B_z$ offset drift | 66 µT | 500 µT | 440 µT |
| Range | 15 mm | n/a | 30 mm |
| Accuracy | 1% | n/a | 1% |
| Stray-field imm. | Yes | Yes | No |

Ferrite magnet). The solution in [21] uses two separate chips with just $B_z$ sensing. Angle calculation is then deferred off-chip. This arrangement has the advantage of offering larger ranges, because the sensitive spots are spread much further on two different chips. In addition to requiring two chips, this solution is not stray-field immune, as the field $B_z$ is measured directly. Hence any stray field along the z-axis is interpreted as a legitimate signal, and there is no rejection factor.

## VII. Conclusions

A new concept for a linear displacement Hall sensor was presented. It consists of two IMC disks, horizontal HEs measuring the left-vs-right change of magnetic field, the signal conditioning, and the needed calculation algorithm. The leakage of the common-mode field dominates the error budget. A joint understanding of the on-chip and application non-idealities is needed to quantify the real-world performance.

We showed that production parts achieve 1% accuracy with practical simple cubic Ferrite 2-pole magnet. Lower errors are achievable with more elaborate magnet designs. The sensor meets the most stringent automotive norms for standalone sensors in harsh environment (in terms of EMC, ESD, stray field, operating temperature …). The demonstrated stray-field immunity makes this solution ready for the vehicle electrification wave.

## References


[1] Y. de Charentenay, "Magnetic sensors market & technologies 2017," Yole, Lyon, France, Tech. Rep., 2017.

[2] A. Vassilev, A. Ferber, C. Wehrmann, O. Pinaud, M. Schilling, and A. R. Ruddle, "Magnetic field exposure assessment in electric vehicles," *IEEE Trans. Electromagn. Compat.*, vol. 57, no. 1, pp. 35–43, Feb. 2015.

[3] S. Nihtianov, "Measuring in the subnanometer range: Capacitive and eddy current nanodisplacement sensors," *IEEE Ind. Electron. Mag.*, vol. 8, no. 1, pp. 6–15, Mar. 2014.

[4] A. Affanni, A. Guerra, L. Dallagiovanna, and G. Chiorboli, "Design and characterization of magnetostrictive linear displacement sensors," in *Proc. 21st IEEE Instrum. Meas. Technol. Conf.*, May 2004, pp. 206–209.

[5] M. Jagiella, S. Fericean, R. Droxler, and A. Dorneich, "New magneto-inductive sensing principle and its implementation in sensors for industrial applications," in *Proc. IEEE Sensors*, vol. 2, Oct. 2004, pp. 1020–1023.

[6] B. Kaviraj and S. K. Ghatak, "Magnetic field and displacement sensor based on giant magneto-impedance effect," *Mater. Manuf. Processes*, vol. 21, no. 3, pp. 271–274, May 2006.

[7] M. Martino, A. Danisi, R. Losito, A. Masi, and G. Spiezia, "Design of a linear variable differential transformer with high rejection to external interfering magnetic field," *IEEE Trans. Magn.*, vol. 46, no. 2, pp. 674–677, Feb. 2010.

[8] R. S. Popovic, *Hall Effect Devices*, 2nd ed. New York, NY, USA: Taylor & Francis, 2003.

[9] L. Jogschies *et al.*, "Recent developments of magnetoresistive sensors for industrial applications," *Sensors*, vol. 15, no. 11, pp. 28665–28689, Nov. 2015.

[10] K. Rohrmann, P. Meier, M. Sandner, and M. Prochaska, "A novel methodology for stray field insensitive xMR angular position sensors," in *Proc. IEEE Sensors*, Oct. 2018, pp. 1–4.

[11] N. Dupré, O. Dubrulle, S. Huber, J. W. Burssens, S. Christian, and G. F. Close, "Experimental demonstration of stray-field immunity beyond 5 mT for an automotive-grade rotary position sensor," in *Proc. Eurosensors*, vol. 2, 2018, p. 763.

[12] *Road Vehicles: Part 8, Immunity to Magnetic Fields*, Standard ISO 11452-8, Jun. 2015.

[13] Z. Lázár, Y. Bidaux, M. Roos, and G. F. Close, "Model-based engineering of magnetic position sensors," in *Proc. Int. Conf. Synth., Modeling, Anal. Simulation Methods Appl. Circuit Design (SMACD)*, Jun. 2019, pp. 105–108.

[14] M. Ortner and L. G. C. Bandeira. *Magpylib: Python Package for Calculating Magnetic Fields of Magnets, Currents and Moments*. Accessed: Jan. 20, 2020. [Online]. Available: Magpylib.readthedocs.io/en/latest/

[15] V. Hiligsmann and P. Riendeau, "Monolithic 360 degrees rotary position sensor IC," in *Proc. IEEE Sensors*, vol. 3, Oct. 2004, pp. 1137–1142.

[16] S. Leroy, S. Rigert, A. Laville, A. Ajbl, and G. F. Close, "Integrated Hall-based magnetic platform for position sensing," in *Proc. 43rd IEEE Eur. Solid State Circuits Conf. (ESSCIRC)*, Sep. 2017, pp. 360–363.

[17] P. Ruther, U. Schiller, W. Buesser, R. Janke, and O. Paul, "Thermomagnetic residual offset in integrated Hall plates," in *Proc. IEEE Sensors*, vol. 2, 2002, pp. 763–766.

[18] H. Husstedt, U. Ausserlechner, and M. Kaltenbacher, "*In-situ* analysis of deformation and mechanical stress of packaged silicon dies with an array of Hall plates," *IEEE Sensors J.*, vol. 11, no. 11, pp. 2993–3000, Nov. 2011.

[19] J. Pascal, L. Hébrard, V. Frick, J.-B. Kammerer, and J.-P. Blondé, "Intrinsic limits of the sensitivity of CMOS integrated vertical Hall devices," *Sens. Actuators A, Phys.*, vol. 152, no. 1, pp. 21–28, May 2009.

[20] C. Sander *et al.*, "Fully symmetric vertical Hall devices in CMOS technology," in *Proc. IEEE Sensors*, Nov. 2013, pp. 1–4.

[21] A. Foletto and A. Friedrich, "Analysis of a Hall-effect system with two linear sensor ICs for 30 mm displacement," Allegro MicroSystems, Manchester, NH, USA. Tech. Rep. 296097-AN, 2013.

[22] *AS5403A/D/E: 3D Hall Position Sensor for Linear and Off-Axis Applications*, ams AG, Premstätten, Austria, 2015.


**Nicolas Dupré** received the joint M.S. degree in micro and nanotechnologies for integrated systems from EFPL, INPG, and PoliTo in 2014. In 2014, he worked on the development of pressure sensors for smartphones with the Research and Development Department, Measurement Specialities. Since 2015, he has been with Melexis, Bevaix, Switzerland. As a development engineer, he works on the development of new magnetic concepts and new magnetic products. He has authored or coauthored several articles and contributed to several conferences.

**Yves Bidaux** received the M.S. degree in physics from EPFL, Lausanne, in 2013, and the Ph.D. degree in physics from ETH Zürich in 2017. From 2013 to 2016, he worked on the development of mid-infrared semiconductor laser sources with the Research and Development Department, Alpes Lasers SA, Neuchâtel, Switzerland. In 2016, he joined the Quantum Optoelectronics Group, ETH Zürich, where he contributed to the development of mode-locked semiconductor lasers. As a senior development engineer, he works on the development of magnetic sensors technologies and products. Since 2017, he has been with Melexis, Bevaix, Switzerland. He has authored or coauthored over 25 articles and conference contributions. He holds one patent.

**Olivier Dubrulle** received the master's degree in electronics engineering from ISEN Engineering School in Lille in 2010.

In 2010, he started as a Test Engineer for magnetic sensors at Melexis. In 2012, he became a Process Engineer, working on automated test equipment and test methodology. Since 2018, as the Industrialization Project Manager, he has been leading a multidisciplinary team, driving the development of manufacturing solutions for integrated circuits, from concept to ramp-up. Since his beginning with Melexis, he has contributed, designed, and implemented test methodology for bipolar and gradiometric magnetic sensors. He holds one pending patent, and he has received the LSSA Green Belt in 2018.

**Gael F. Close** (Senior Member, IEEE) received the B.Sc.Eng. degree in electrical engineering from the University of Liège, Liège, Belgium, in 2003, and the M.S. and Ph.D. degrees in electrical engineering from Stanford University, Stanford, CA, USA, in 2004 and 2008, respectively. From 2008 to 2011, he was with IBM Research, Zürich, Switzerland, developing phase-change memory chips. Since 2011, he has been with Melexis, Bevaix, Switzerland. As a senior system engineer, he leads the technical development of the magnetic sensor product line. He has published about 30 peer-reviewed publications in international journals and conferences, covering nano-electronic devices, circuit/system design, and sensor product development. He holds one patent, and received an IASCC Six Sigma Black Belt in 2017.